






Nuclearity enlargement from $[PW_9O_{34}@Ag_{51}]$ to $[(PW_9O_{34})_2@Ag_{72}]$ and 2D and 3D network formation driven by bipyridines

Zhi Wang ¹, Yan-Jie Zhu¹, Ying-Zhou Li ², Gui-Lin Zhuang ³, Ke-Peng Song ¹, Zhi-Yong Gao⁴, Jian-Min Dou⁵, Mohamedally Kurmoo⁶, Chen-Ho Tung¹ & Di Sun ¹✉

The structural transformations of metal nanoclusters are typically quite complex processes involving the formation and breakage of several bonds, and thus are challenging to study. Herein, we report a case where two lacunary Keggin polyoxometallate templated silver single-pods $[PW_9O_{34}@Ag_{51}]$ (SD/Ag51b) fuse to a double-pod $[(PW_9O_{34})_2@Ag_{72}]$ by reacting with 4,4'-bipyridine (bipy) or 1,4-bis(4-pyridinylmethyl)piperazine (pi-bipy). Their crystal structures reveal the formation of a 2D 4⁴-*sql* layer (SD/Ag72a) with bipy and a 3D *pcu* framework (SD/Ag72c) with pi-bipy. The $PW_9O_{34}^{9-}$ retains its structure during the cluster fusion and cluster-based network formation. Although the two processes, stripping of an Ag-ligands interface followed by fusion, and polymerization, are difficult to envisage, electrospray ionization mass spectrometry provides enough evidences for such a proposal to be made. Through this example, we expect the structural transformation to become a powerful method for synthesizing silver nanoclusters and their infinite networks, and to evolve from trial-and-error to rational.

¹School of Chemistry and Chemical Engineering, and State Key Laboratory of Crystal Materials, Shandong University, 250100 Ji'nan, People's Republic of China. ²Shandong Provincial Key Laboratory of Molecular Engineering, Qilu University of Technology (Shandong Academy of Science), 250353 Ji'nan, People's Republic of China. ³College of Chemical Engineering and Materials Science, Zhejiang University of Technology, 310032 Hangzhou, People's Republic of China. ⁴School of Chemistry and Chemical Engineering, Henan Normal University, 453007 Xinxiang, People's Republic of China. ⁵Shandong Provincial Key Laboratory of Chemical Energy Storage and Novel Cell Technology and School of Chemistry and Chemical Engineering, Liaocheng University, 252000 Liaocheng, People's Republic of China. ⁶Université de Strasbourg, Institut de Chimie de Strasbourg, CNRS-UMR 7177, 4 rue Blaise Pascal, 67008 Strasbourg, Cedex, France. ✉email: dsun@sdu.edu.cn

The ubiquity of coordination-dissociation equilibrium of metal clusters in solution with partial retention of their original connectivity within the molecular structure provides a way to change their nuclearities and in some cases, allow for oligomerization to giant homologs^{1–6}. Because of the subtle balance of bond energies, for example Ag–S, Ag–N, Ag–O versus Ag...Ag, and geometrical shapes, these reactions have given rise to an unexpected chemistry where coordination rules are not always fully obeyed and is now developing in a preparation process hereafter called structural transformation of metal nanoclusters. This process has been used to create clusters in a more controllable way compared to the classical de novo synthesis of cluster from simple reactants^{7–13}. In particular, structural transformation is especially adapted for the assembly of silver clusters because of the versatile coordination geometries of Ag atom (strong coordination bonds) and ubiquitous moderate to weak argentophilic interactions as well as weak hydrogen bonding interactions^{14–18}. Such alliance of pre-existing strong and weak interactions in silver clusters favors their subsequent dynamic structure transformation in response to some stimuli while partially retaining the cluster nuclearity, structure and at times its geometry. Currently, the employment of such strategy in the syntheses of silver clusters remains a rare event, although a related one called LEIST (ligand-exchange-induced size/structure transformation) methodology has been developed for reduced Au nanoclusters^{19–22}. Related to structural transformation, Mak's group revealed an induced silver core enlargement from a small Cl@Ag₁₄ to a large Cl₆Ag₈@Ag₃₀ by the reaction with AgClO₄²³. Soon afterwards, a discrete Ag₁₂ cluster was interconnected into a 3D framework by post-synthetic modification using 4,4'-bipyridine (bipy), while the unchanged silver cluster acts as the secondary building unit in the polymerization process²⁴. Zang's group reported the reversible configuration transformation of the [V^V₁₀V^{IV}₂O₃₄]^{10–} core in the Ag₃₀ nanocage upon acid/base stimuli²⁵. These sporadic reports exemplified the potential of structural transformation of silver clusters by specific stimuli. Motivated by the above advances, our group also successfully realized the synergetic conversion of both core and shell from [Mo₆O₂₂@Ag₄₄] to [Mo₈O₂₈@Ag₅₀] induced by benzoic acid and deciphered the underlying breakage-growth-reassembly (BGR) transformation mechanism based on a comprehensive characterization using electrospray ionization mass spectrometry (ESI-MS)²⁶. This is a very complex and unique structural transformation involving the simultaneous enlargement of both the anionic core template and the outer silver shell.

As an important subclass of polyoxometalates (POMs), lacunary POMs have more O binding sites, higher negative charges and pre-organized region containing asymmetric metal-accessible vacant sites^{27–30}, thus should be a kind of powerful anion template to assemble silver clusters. Nonetheless, lacunary POMs templated silver clusters are very seldom which may be caused by the instability of lacunary POMs in solution. Hitherto, only few examples have appeared based on such kind of POMs, [(PW₉O₃₄)₂@Ag₇₀]³¹, [(PW₉O₃₄)₂@Ag₆₇]³², [α-SiW₁₀O₃₇@Ag₄₁]³³, and [SiW₉O₃₄@Ag₅₁]³⁴. Of note Wang et al. introduced the ionothermal synthesis to address the stability problem of lacunary POMs during the assembly of silver clusters³¹.

In this work, we isolated a pumpkin-like single PW₉O₃₄^{9–} templated Ag₅₁ cluster, [(PW₉O₃₄)@Ag₅₁(iPrS)₂₅(CF₃COO)₁₇(DMF)₃(CH₃OH)₃] (SD/Ag51b) using a straightforward synthesis method. The coordination of six solvent molecules on the surface of SD/Ag51b inspired us to apply structural transformation by employing bridging poly-pyridine ligands such as bipy and 1,4-bis(4-pyridinylmethyl)piperazine (pi-bipy). As expected, a 2D 4⁴-sq^l layer {[(PW₉O₃₄)₂@Ag₇₂S(iPrS)₄₁(CF₃COO)₈(bipy)_{5.5}(CH₃OH)(H₂O)]·3CF₃COO}_n (SD/Ag72a) and a 3D *pcu* framework

{[(PW₉O₃₄)₂@Ag₇₂S(iPrS)₄₂(CF₃COO)₇(pi-bipy)_{4.5}(CH₃OH)]·3CF₃COO}_n (SD/Ag72c) containing peanut-like double PW₉O₃₄^{9–} templated 72-nuclei silver cluster as node were isolated. Such structural transformation examples involve the simultaneous increase of the nuclearity of the silver cluster and network formation of different dimensionalities induced by two closely related bipy.

Results

Synthesis. Colorless block crystals of SD/Ag51b are formed from the reaction of (iPrSAg)_n, CF₃COOAg, and Na₉(A-PW₉O₃₄)·7H₂O in CH₃OH/DMF at 25 °C. Subsequent addition of bipy to the mother liquor of above reaction system yields light yellow needles of SD/Ag72a (Fig. 1). Also reaction of bipy with crystals of SD/Ag51b dissolved in CH₃OH leads to SD/Ag72a (Fig. 1). But if the bipy is added before the formation of SD/Ag51b, SD/Ag72a is not obtained. This confirms that the preformed SD/Ag51b is the key precursor to SD/Ag72a while partially retaining its molecular structure (see below). This is also in line with ESI-MS results (see later). We can then stress that structural transformation is indispensable for generating crystalline silver clusters that are unreachable using traditional one-pot reaction. We also tried to respectively add 1,4-bis(pyrid-4-yl)benzene and pi-bipy to the methanol solution of SD/Ag51b, but only latter gave brown-yellow crystals of SD/Ag72c (Supplementary Fig. 2). A sequence of characterization techniques such as Fourier transform-infrared spectroscopy (FTIR), UV-Vis spectroscopy, DFT calculations, fluorescence spectroscopy, energy-dispersive X-ray spectroscopy (EDS), single-crystal X-ray diffraction (SCXRD), and powder X-ray diffraction (PXRD), were used in this system (Supplementary Figs. 20–38).

X-ray structures of SD/Ag51b and SD/Ag72a. SCXRD of SD/Ag51b (triclinic, space group *P*-1) found a complete cluster as the asymmetric unit. It can be described as a multishell ball consisting of {PO₄}@{WO₆}₉@Ag₅₁@ligands with a cross-section of 1.1 × 1.4 nm² excluding the outer ligands. Based on the molecular building units and for simplicity, we describe it as a single-pod with a core (POM, PW₉O₃₄^{9–}) wrapped by the shell (Ag-ligands). The PW₉O₃₄^{9–} core retains its structure as in Na₉(A-PW₉O₃₄)·7H₂O (Figs. 2a, b). This lacunary Keggin POM acts as template for the pumpkin-like Ag₅₁ shell (Figs. 2c, d) through Ag–O interactions (2.30–2.79 Å) involving coordination to a total of 37 Ag atoms (Supplementary Fig. 3). The silver coordination numbers, not including Ag...Ag contact, vary from 3 (T or Y shape), 4 (seesaw or tetrahedron) to 5 (square-pyramid) (Supplementary Fig. 4). There are 25 iPrS[–], 17 CF₃COO[–], 3 terminal DMF and 3 CH₃OH bonded to and protecting the silver shell. All iPrS[–] show a μ₄ mode through the sulfur except for two μ₃-iPrS[–] (Ag–S = 2.32–2.88 Å), and the 17 CF₃COO[–] show four different coordination modes (μ₁-κ¹:κ⁰, μ₂-κ¹:κ¹, μ₃-κ¹:κ², and μ₄-κ¹:κ³; Ag–O = 2.19–2.78 Å). The silver shell is further consolidated by numerous argentophilic interactions (Ag...Ag = 2.84–3.41 Å). It is an example where the PW₉O₃₄^{9–} is individually wrapped by a silver shell, in contrast to being in pairs in Ag₇₀³¹ and Ag₆₇ clusters³².

The presence of six coordinated solvent molecules on the surface of Ag₅₁ shell (Supplementary Fig. 5) prompted us to explore the possibility of using it as a secondary building unit in extending to polymeric structures. We therefore used bipy as a ditopic connector and successfully isolated a 4⁴-sq^l network (SD/Ag72a) but with an unexpected modification to the pristine SD/Ag51b cluster where it has gone from a single-pod to a double-pod one. SCXRD of SD/Ag72a (monoclinic *P*2₁/*n*) reveals a double-pod cluster with face-to-face POMs centered by a S^{2–} ion as template. The molecular cross-sectional dimension is 2.1 × 1.0 nm² excluding the ligands. The

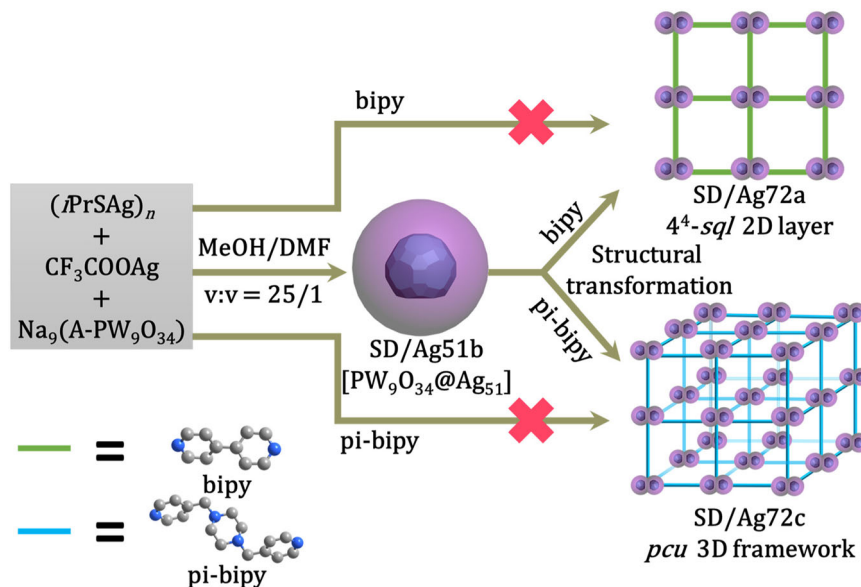


Fig. 1 Schematic representation of the structural transformation of SD/Ag72a and SD/Ag72c from SD/Ag51b. Upper: The bipy induced SD/Ag51b to form 4⁴-sql 2D layer of SD/Ag72a. Lower: The pi-bipy induced SD/Ag51b to form 3D pcu framework of SD/Ag72c.

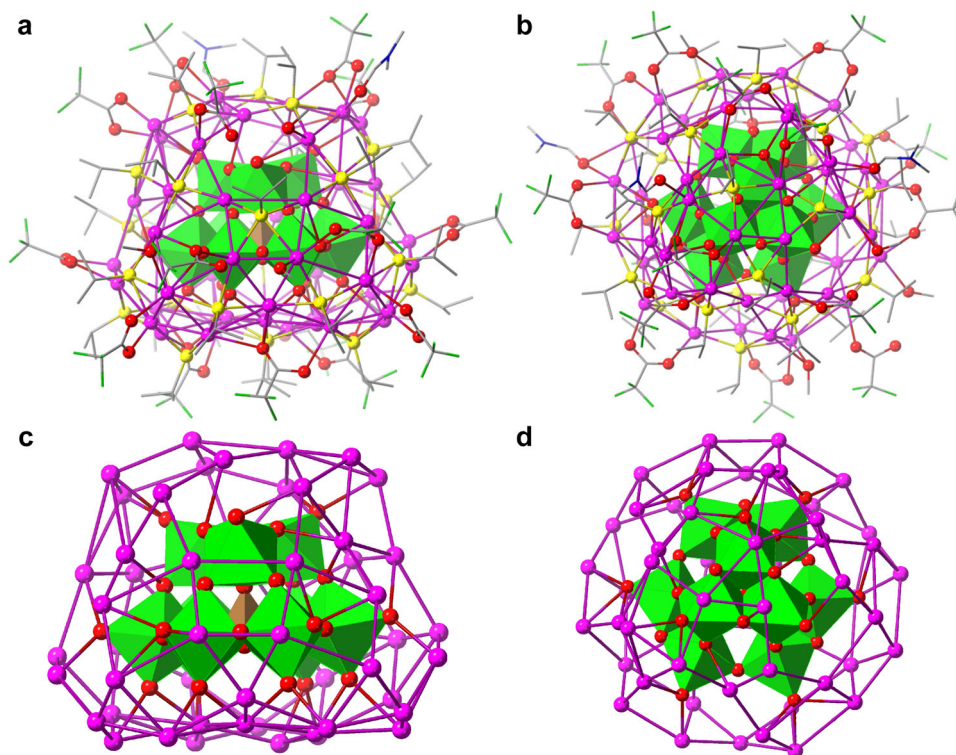


Fig. 2 Crystal structure of SD/Ag51b. **a, c** Side and **(b, d)** top views including (top) and excluding (bottom) the ligands. Color labels: purple, Ag; blue, N; yellow, S; gray, C; red, O; green, F. All H atoms are omitted. $\text{PW}_9\text{O}_{34}^{9-}$ is shown in polyhedral mode with PO_4 and WO_6 colored as brown and green.

asymmetric unit has a complete peanut-like 72-nuclei silver cluster, which is protected by 41 $i\text{PrS}^-$ (μ_3 and μ_4 ; Ag-S = 2.29–2.93 Å), 8 CF_3COO^- ($\mu_1\text{-}\kappa^1\text{:}\kappa^0$ and $\mu_2\text{-}\kappa^1\text{:}\kappa^1$; Ag-O = 2.21–2.71 Å), 11 bipy (Ag-N = 2.26–2.38 Å) as well as coordinated CH_3OH and H_2O (Fig. 3a). The coordination numbers of silver atoms are now extended to 2 (linear), 3 (T or Y shape), 4 (seesaw or tetrahedron), 5 (square-pyramid) and 6 (octahedron) (Supplementary Fig. 6). The Ag_{72} cluster comprises two hemispheres of Ag_{29} and Ag_{31} sandwiching an equatorial S^{2-} -centered Ag_{12} plane (Fig. 3b and Supplementary Fig. 7). In each silver hemisphere, a $\text{PW}_9\text{O}_{34}^{9-}$ is

encapsulated as template which supports the outer shell and connects the equatorial $\text{S}@\text{Ag}_{12}$ plane using the lacunary face of the $\text{PW}_9\text{O}_{34}^{9-}$. There are 52 of 72 Ag coordinated to two $\text{PW}_9\text{O}_{34}^{9-}$ through Ag-O bonds (2.29–2.79 Å). The structure of $\text{PW}_9\text{O}_{34}^{9-}$ in SD/Ag72a is the same as that in SD/Ag51b, indicating the robustness of $\text{PW}_9\text{O}_{34}^{9-}$ even after experiencing transformation reaction. Importantly, each $[(\text{PW}_9\text{O}_{34})_2@(\text{Ag}_{72})]$ cluster is connected to four neighbors through a total of 11 bridging bipy (Fig. 3c) to form a 2D 4⁴-sql network (Fig. 3d and Supplementary Fig. 8). The two take-away information from these observations are (a) the

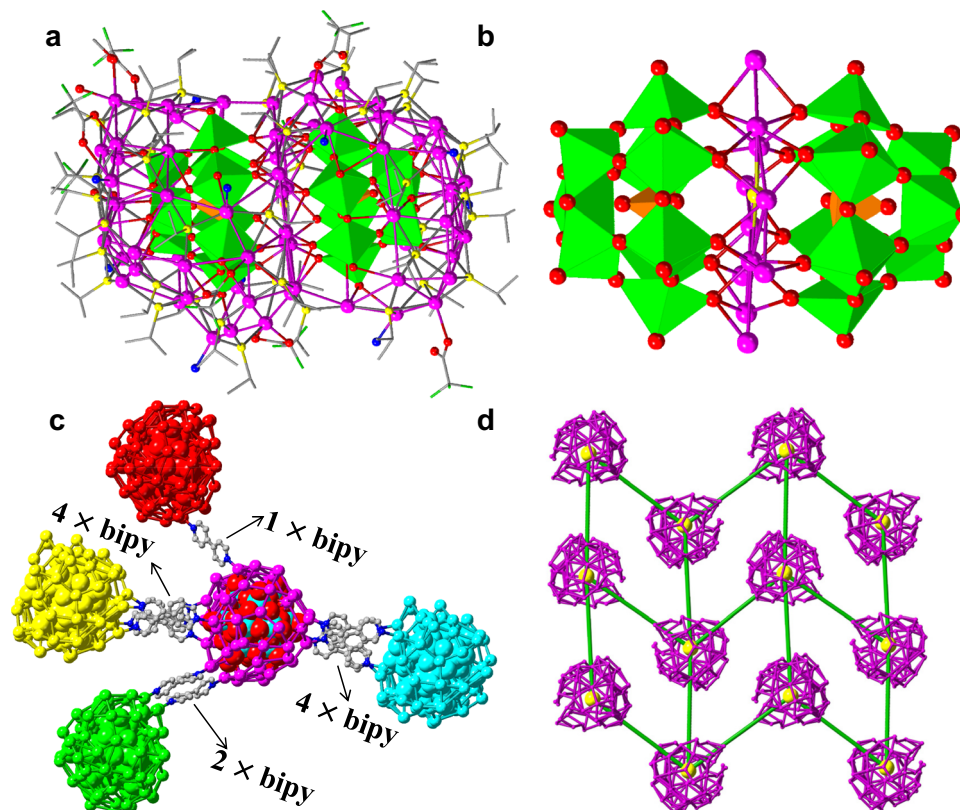


Fig. 3 Crystal structure of **SD/Ag72a**. **a** $[(PW_9O_{34})_2@Ag_{72}]$ cluster with the ligands and **(b)** highlighting the sandwiched S^{2-} -centered silver plane by two $PW_9O_{34}^{9-}$. Color labels: same as Fig. 1. Only N atoms of coordinated bipy are shown for clarity. **c** The connections between $[(PW_9O_{34})_2@Ag_{72}]$ clusters. $PW_9O_{34}^{9-}$ is shown in space-filling mode. **d** The simplified 2D 4^4 -sq network with $[(PW_9O_{34})_2@Ag_{72}]$ as node (yellow balls) and bipy as linker (green sticks).

structural transformation of a low nuclearity silver cluster to a higher one while retaining its templating POM intact but with a slightly modified Ag shell, and (b) the connection of these clusters, as secondary building units, by the ditopic bipy to a coordination polymer.

Of note **SD/Ag72a**, $[(PW_9O_{34})_2@Ag_{72}]$, is the largest PW_9O_{34} -templated silver cluster so far, followed by $[(PW_9O_{34})_2@Ag_{70}]$ ³¹ and $[(PW_9O_{34})@Ag_{67}]$ ³². Their similarities and differences give interesting information in the field of giant silver clusters. Their overall geometric shapes which are dominated by that of the templated POM are almost the same and they are all double-pods with two cores (POM , $PW_9O_{34}^{9-}$) wrapped by the shell (Ag-ligands). The major differences appear in the Ag-ligand shells (Supplementary Fig. 9). To simplify the discussion we define two parts: one is separator between the two pods and the other is the outer hemisphere. For $[(PW_9O_{34})_2@Ag_{70}]$ the separator is an almost flat plane of Ag_{10} and the hemispheres are equal consisting of Ag_{30} . For $[(PW_9O_{34})_2@Ag_{67}]$ the separator is Ag_{12} and the hemispheres are unequal, Ag_{28} and Ag_{27} . **SD/Ag72a** has a centrally placed S^{2-} within an Ag_{12} as separator. In spite of the structurally undisturbed anion template, the differences in the overall silver skeletons are likely driven by the capping ligands with different electronic and steric effects, such as $iPrS^-$, CF_3COO^- , bipy for **SD/Ag72a**, $tBuC\equiv C^-$ for $[(PW_9O_{34})_2@Ag_{70}]$ and p -F- PhS^- , CF_3COO^- for $[(PW_9O_{34})_2@Ag_{67}]$. Other factors include the divergence of the bipy and supramolecular interactions.

Structure transformation from SD/Ag51b to SD/Ag72a. The structural transformation procedure indicates the formation of **SD/Ag72a** is only possible after the formation of **SD/Ag51b**; that is introduction of bipy to the mother liquor or following isolation and

subsequent reaction (Supplementary Fig. 1). Furthermore, using bipy as a reactant before the formation of **SD/Ag51b** gave negative results. Thus, regardless of the route taken, it is important to verify the stability of **SD/Ag51b** in CH_3OH , which guarantees the transformation reaction genuinely started from Ag_{51} cluster rather than from some fragmented silver species in solution. We performed an ESI-MS study since it has been demonstrated to be a powerful tool to investigate stability and the assembly process of coordination compounds^{35–42}. The positive-ion mode ESI-MS of **SD/Ag51b** dissolved in CH_3OH (Fig. 4a) presents seven key doubly-charged peaks in the m/z range 2000–7000. The strongest peak (**1c**; $m/z = 5652.40$) corresponds to a complete cluster $[(PW_9O_{34})@Ag_{51}(iPrS)_{25}(CF_3COO)_{15}]^{2+}$ (Calcd. $m/z = 5652.48$), which is formed by losing 2 CF_3COO^- and solvent molecules. All other peaks were assigned with precise formulae (Supplementary Table 1) and matched well with their simulated isotopic distributions (Inset of Fig. 4a). The $\Delta m/z$ for the pairs **1a–1b**, **1b–1c**, **1c–1d**, **1e–1f**, **1f–1g** are ca. 110, which equals the mass of CF_3COOAg divided by charge state (+2), and indicates the progressive gain of CF_3COOAg . The peak (**1e**; $m/z = 5821.55$) can be seen as a solvate addendum of **1d** and identified to be $[(PW_9O_{34})@Ag_{52}(iPrS)_{25}(CF_3COO)_{16}(H_2O)_3(CH_3OH)_2]^{2+}$ (Calcd. $m/z = 5821.47$). There is no bigger fragment, ruling out the possibility of solvent-induced formation of **SD/Ag72a**. The ESI-MS of the reaction mother solutions during the synthesis of **SD/Ag51b** shows the same peaks **1a**, **1b**, **1c** and **1d** but of low intensities (Supplementary Fig. 10), which suggest that formation and fragmentation follow the same fashion to mentioned above. Furthermore, **SD/Ag51b** can be recrystallized from CH_3OH (Supplementary Fig. 11). These results confirm: (i) **SD/Ag51b** retains the integrity of its metallic skeleton in CH_3OH , (ii) **SD/Ag51b** exists in slightly different forms in solution through surface coordination/

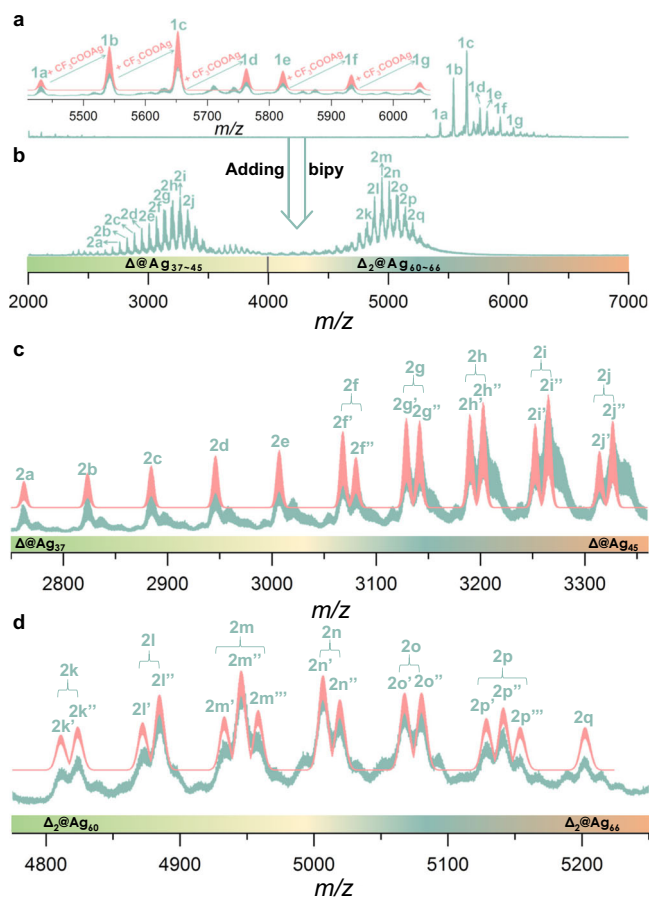


Fig. 4 Electro spray ionization mass spectrometry (ESI-MS) of SD/Ag51b before and after adding bipy. Positive-ion ESI-MS of SD/Ag51b dissolved in CH₃OH before (a) and after adding bipy (b); Δ = PW₉O₃₄⁹⁻. The charge states for all labeled species in (a) and (b) are +2 and +3, respectively. Inset: The expanded experimental (green line) and simulated (red line) isotope-distribution patterns of 1a–1g. The expanded experimental (green line) and simulated (red line) isotope-distribution patterns of 2a–2j (c) and 2k–2q (d).

disassociation of the labile ligands, (iii) SD/Ag72a can only be obtained from SD/Ag51b using a structural transformation way.

The most intriguing question that arises from the structural transformation is how SD/Ag51b transforms to SD/Ag72a after adding bipy to the solution? ESI-MS provide such insights into the evolution of solution species. Introduction of bipy into a methanol solution of SD/Ag51b initiated a synchronous cluster destruction and growth, which are revealed by two separated groups of +3 charged peaks before and after $m/z = 4000$, respectively (Fig. 4b). Below $m/z = 4000$, a total of ten peaks originating from 15 different species were identified (Fig. 4c). All contain a single PW₉O₃₄⁹⁻ template enwrapped by a shell smaller than Ag₅₁, (PW₉O₃₄)₂@Ag_{37–45}. Among them, the most dominant species of 2i'' can be assigned to [(PW₉O₃₄)₂@Ag₄₄(iPrS)₂₂(CF₃COO)₁₀(H₂O)₂]³⁺. Each grouped peak in 2f–2j contains two overlapped species with one iPrS⁻ in former replaced by one CF₃COO⁻ in latter. Above $m/z = 4000$, another 15 species overlapping in seven peaks were assigned to double PW₉O₃₄⁹⁻ templated clusters of nuclearity higher than 51, (PW₉O₃₄)₂@Ag_{60–66} (Fig. 4d). They are very likely intermediates towards Ag₇₂. The main species in this group are (PW₉O₃₄)₂@Ag₆₂ having different iPrS⁻:CF₃COO⁻ ratios (2m', 2m'', and 2m'''). All thirty species were precisely assigned based on simulated and observed isotopic patterns (Supplementary Table 2). The result indicates the lability of the ligands allows for their rapid exchange

which promotes the silver shell of SD/Ag51b to be dynamic to the formation of the intermediates toward the final SD/Ag72a. In comparison with the plenary POMs, the PW₉O₃₄⁹⁻ possesses more bare-oxygen vacancies and a higher negative charge, therefore, the W₆ face at the base of the pumpkin-like Ag₅₁ cluster may be more active and have higher affinity with the silver atoms than the W₃ face. Correspondingly, the silver atoms attached to the W₆ face are also endowed with high reactivity. These highly active regions may be preferentially chosen the way of face-fusion to form a stable entity. Combined with the above observations, we proposed a bipy-induced breakage-fusion conversion mechanism for this system (Fig. 5). The successful isolation of SD/Ag72a is caused by the disappearance of the smaller SD/Ag51b and this kind of fusion represents a simple model to explain usual coalescence of surfactant-protected nanoparticles from discrete nanocrystals or nanoclusters. The structural transformation was further elucidated by the HAADF-STEM, where the size of the nanoparticles increased from approximately 1.3 to 2.1 nm and some aggregation behavior of them were observed after adding bipy to the methanol solution of SD/Ag51b (Supplementary Fig. 12).

The ³¹P NMR was also performed to verify this question (Supplementary Fig. 13). A single resonance peak at $\delta = -10.24$ ppm corresponding to PO₄³⁻ was observed for SD/Ag51b dissolved in methanol, corroborating with one crystallographically independent PW₉O₃₄⁹⁻. However, the resonance signal of PO₄³⁻ completely disappear in the -350 to 250 ppm range after adding bipy with the color changing from colorless to yellow. When ejecting the NMR tube from instrument, we surprisingly found abundance of tiny crystals precipitated from the solution, which were confirmed to be SD/Ag72a by unit cell checking on a single crystal X-ray diffractometer (Supplementary Fig. 14). The formation of insoluble SD/Ag72a decreased the concentration of PO₄³⁻-containing species in solution, as a result, no signal can be detected after conversion reaction. All these results unambiguously evidenced the occurrence of cluster conversion reaction by addition of bipy.

Universality of bipy-induced transformation. Followed by above successful case, we further evidenced the universality of structural transformation strategy and isolated SD/Ag72c as a *pcu* framework by adding pi-bipy to the methanol solution of SD/Ag51b. SCXRD analysis shows that the asymmetric unit in SD/Ag72c is very similar to that in SD/Ag72a (Supplementary Fig. 15). Differently, each [(PW₉O₃₄)₂@Ag₇₂] cluster in SD/Ag72c is connected to six neighbors through a total of 9 bridging pi-bipy ligands (Fig. 6a) to form a 3D *pcu* framework (Fig. 6b).

UV-Vis absorption spectra and luminescence properties. The solid-state UV/Vis spectra of SD/Ag51b and SD/Ag72a at room temperature are shown in Supplementary Fig. 16. Both exhibit single intense absorption centered at 341 and 352 nm, respectively. Given their structural relevance, the structurally simplified model SD/Ag51b was used as a representative to analyze their electronic transitions by means of TD-DFT calculations (See details in Supplementary Information). The absorptions above 400 nm can be ascribed to the ligand and metal charge transfer to the inner core (herein named after L[C]CT and M[C]CT, respectively), i.e. transitions from the surface ligands (mainly 3p orbitals of S atoms in the thiol ligands and 2p orbitals of O atoms in the carboxylic ligands) and Ag atoms (mainly 4d orbitals) to the W = O π^* orbitals (formed by 5d orbitals of W atoms and 2p orbitals of O atoms) in the inner PW₉O₃₄ core; such type of transitions were also previously found in some molybdate-templated Ag clusters²⁶. Another two types of transitions, such as those from Ag 4d to its 5s/p orbitals (MMCT, metal to metal

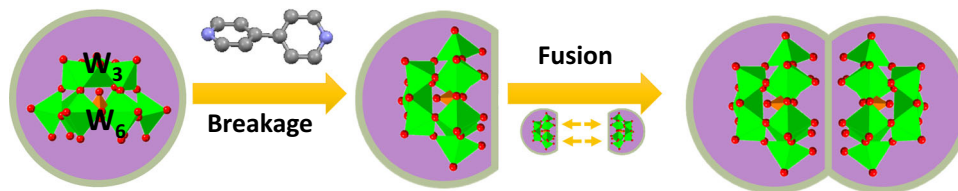


Fig. 5 Proposed breakage-fusion conversion mechanism from SD/Ag51b to SD/Ag72a. The green shell represents silver shell.

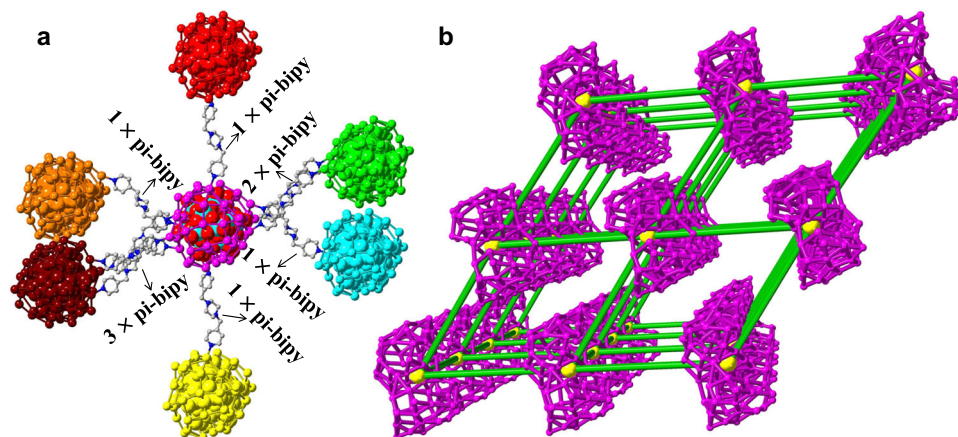


Fig. 6 Crystal structure of SD/Ag72c. **a** The connections between $[(PW_9O_{34})_2@Ag_{72}]$ clusters in SD/Ag72c. $PW_9O_{34}^{9-}$ is shown in space-filling mode. **b** The simplified 3D *pcu* framework with $[(PW_9O_{34})_2@Ag_{72}]$ as node (yellow balls) and pi-bipy as linker (green sticks).

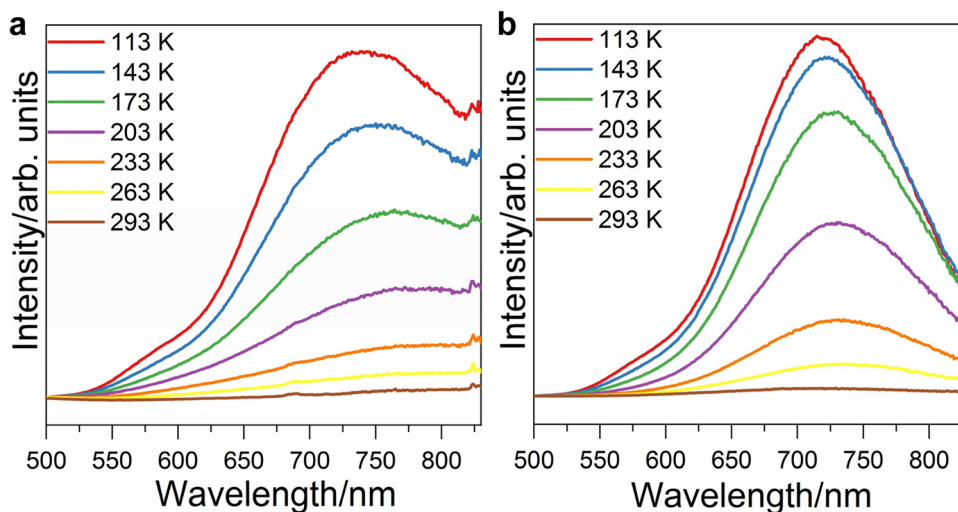


Fig. 7 Luminescence spectra of SD/Ag51b and SD/Ag72a. Variable-temperature emission spectra for SD/Ag51b (**a**) and SD/Ag72a (**b**).

charge transfer) and those from surface *S/O p* orbitals to Ag *5 s/p* orbitals (LMCT, ligand to metal charge transfer), also becomes apparent in the higher-energy region, as exemplified by the typical transitions of HOMO-4/HOMO-6→LUMO + 9 and HOMO-13→LUMO + 3 (Supplementary Table 3 and Data 1). The calculated UV spectrum shows an absorption maximum at 338 nm, which is in fair agreement with the experimental value (300 nm) of SD/Ag51b (Supplementary Fig. 17).

The experimental variable-temperature (113–293 K) solid state emission spectra of SD/Ag51b and SD/Ag72a under the excitation of 468 nm are shown in Fig. 7. Both emit luminescence in the near-infrared (NIR) region when the temperature is cooling to 263 K with emission peaking at 787 and 737 nm, respectively. Their emission peaks gradually blue-shift to 740 nm for SD/Ag51b and 716 nm for SD/Ag72a upon cooling to 113 K

along with the increase of intensity. The quantum yields of SD/Ag51b and SD/Ag72a at 113 K were measured to be 1.26% and 2.17%, respectively. The average lifetimes of the emissions are also determined to be on the microsecond scale ($\tau = 219.4 \mu\text{s}$ for SD/Ag51b and $\tau = 208.1 \mu\text{s}$ for SD/Ag72a), respectively (Supplementary Fig. 18), indicating their phosphorescence character⁴³. Supplementary Fig. 19 shows good linearity correlation between maximum emission intensity (I_{max}) and temperature (T) in the ranges of 113–233 K (SD/Ag51b) and 113–293 K (SD/Ag72a), which indicate both of them may be promising materials for low-temperature molecular luminescent thermometer. Due to the restriction of theoretical method and computational cost, it is nearly impossible to utilize TD-DFT or other ab-initio method to identify emission mechanism (e.g. electronic transitions, quantum yield) for such larger clusters of SD/Ag51b and SD/Ag72a with

more than 300 non-H atoms. Fortunately, studying electronic transitions of UV absorption is helpful to understand emission property. Based on the calculated absorption results, the emissions of **SD/Ag51b** and **SD/Ag72a** should be associated with the above three types of charge transfers, though the exact excitation/relaxation pathway is still difficult to be determined. According to the previous findings, however, these NIR emissions is more likely to be attributed to the ligand-to-metal charge transfer (LMCT) from S/O *p* to Ag 5 *s/p* orbitals perturbed by Ag...Ag interaction^{44, 45}. The lowest-energy electronic excitation of the model **SD/Ag51b** in gaseous phase, relevant to its fluorescent emission, is calculated to occur at 474 nm and mainly contributed by the transition from HOMO to LUMO. However, the absorption spectrum of **SD/Ag51b** both experimentally and theoretically in solid state shows a longer-wavelength tail beyond 500 nm. It is demonstrated that a lower excitation energy is sufficient to trigger the transition of $S_0 \rightarrow S_1$ in solid state and then gives rise to a longer-wavelength emission by further relaxation of S_1 . In this regard, the NIR emissions in **SD/Ag51b** and **SD/Ag72a** are reasonable and can be partially rationalized by the intermolecular interactions in solid state, which often leads to significant red-shift for the emission by forming possible excimers^{46–48}.

Discussion

The key message of this work is the successful application of the structural transformation from an isolated $PW_9O_{34}^{9-}$ templated single-pod Ag_{51} cluster to a double-pod Ag_{72} cluster by the stimulus of bipy while partially retaining the original bonding, shape and the template. Importantly, the linkers bipy and pi-bipy connect the generated Ag_{72} into a 2D corrugated polymeric sheet and a 3D framework, respectively. Thus, the Ag_{51} cluster can be viewed as an intermediate en-route to larger progeny. The structural transformation involves the increase of the nuclearity of silver cluster by trapping more POM templates and the extension of the discrete cluster to infinite 2D and 3D coordination networks by installing the exotic linkers. A breakage-fusion conversion mechanism was also established via reaction monitoring by ESI-MS. This work not only establishes a well-controlled method for synthesizing larger silver nanoclusters but also deepens our understanding on the structural variability and chemical reactivity of this class of silver clusters.

Methods

Synthesis of (*i*PrSag)_{*n*}. (*i*PrSag)_{*n*} was prepared by the following reported procedure⁶. The solution of $AgNO_3$ (30 mmol, 5.1 g) in 75 mL acetonitrile was mixed with 100 mL ethanol containing *i*PrSH (30 mmol, 2.8 mL) and 5 mL Et_3N under stirring for 3 h in the dark at room temperature, then the yellow powder of (*i*PrSag)_{*n*} was isolated by filtration and washed with ethanol and ether, then dried in the ambient environment (yield: 97 %).

Synthesis of $Na_9(A-PW_9O_{34}) \cdot 7H_2O$. $Na_9(A-PW_9O_{34}) \cdot 7H_2O$ was prepared by the following reported procedure⁴⁹. $Na_2WO_4 \cdot 2H_2O$ (0.36 mol, 120 g) was dissolved in 150 g of water and phosphoric acid (85%) was added dropwise with stirring (0.06 mol, 4.0 mL). After addition of the acid is complete, the measured pH was 8.9 to 9.0. Glacial acetic acid (0.40 mol, 22.5 mL) was added dropwise with vigorous stirring. Large quantities of white precipitate form during the addition. The final pH of the solution was 7.5 ± 0.3 and the precipitate is collected after the solution stirring for 1 h then dried in air (yield: 86%).

Synthesis of **SD/Ag51b.** (*i*PrSag)_{*n*} (0.05 mmol, 9.2 mg) and $Na_9(A-PW_9O_{34}) \cdot 7H_2O$ (0.003 mmol, 7.7 mg) were dissolved in MeOH:DMF (5 mL, v/v = 25:1). After stirring the solution for 1 h at 700 r/min, CF_3COOAg (0.18 mmol, 39.8 mg) was added and the reaction continued for 3 h under the same condition. The colorless solution was filtrated and the filtrate was evaporated slowly in darkness at room temperature. Colorless block crystals were obtained in 63% yield after 1 week. Selected IR peaks (cm^{-1}): 3687 (w), 2959 (w), 1644 (m), 1516 (w), 1449 (w), 1371 (m), 1242 (w), 1195 (m), 1135 (m), 1045 (m), 1033 (m), 884 (w), 830 (m), 797 (m), 712 (s), 599 (m), 498 (w).

Synthesis of **SD/Ag72a.** To the mother solution of **SD/Ag51b**, 4,4'-bipyridine (0.16 mmol, 25 mg) was added and stirred for 3 h. The colorless solution was filtrated and the filtrate was evaporated slowly in darkness at room temperature. Faint yellow crystals were obtained in 20% yield after 1 week. Selected IR peaks (cm^{-1}): 2950 (w), 1952 (m), 1237 (w), 1199 (m), 1127 (m), 1051 (m), 996 (w), 902 (w), 776 (s), 717 (s), 691 (s), 610 (m), 506 (m).

Synthesis of **SD/Ag72c.** To the methanol solution of **SD/Ag51b**, 1,4-bis(4-pyridinylmethyl)piperazine (0.04 mmol, 10 mg) was added and stored in darkness at room temperature. Brown yellow block crystals were obtained in 27% yield after 1 week. Selected IR peaks (cm^{-1}): 2948 (w), 1656 (m), 1606 (w), 1420 (w), 1360 (w), 1241 (w), 1196 (m), 1130 (m), 1045 (w), 903 (w), 828 (w), 775 (s), 693 (s), 608 (m), 507 (m).

Single crystal X-ray diffraction analyses. Single crystals of **SD/Ag51b**, **SD/Ag72a** and **SD/Ag72c** with appropriate dimensions were chosen under an optical microscope and quickly coated with high vacuum grease (Dow Corning Corporation) to prevent decomposition. Each crystal was mounted on CryoLoop™ loop and the cell parameters and intensity data were recorded on a Rigaku Oxford Diffraction XtaLAB Synergy-S diffractometer equipped with a HyPix-6000HE Hybrid Photon Counting (HPC) detector operating in shutterless mode and an Oxford Cryosystems Cryostream 800 Plus at 100 K using Cu K α ($\lambda = 1.54184 \text{ \AA}$) for **SD/Ag51b** and **SD/Ag72c** and Mo K α ($\lambda = 0.71073 \text{ \AA}$) for **SD/Ag72a** from Photonjet micro-focus X-ray Source. Data were processed using the *CrystAlisPro* software suite⁵⁰. These structures were solved using the charge-flipping algorithm, as implemented in the program *SUPERFLIP*⁵¹ and refined by full-matrix least-squares techniques against F_o^2 using the SHELXL program⁵² through the OLEX2 interface⁵³. Hydrogen atoms at carbon were placed in calculated positions and refined isotropically by using a riding model. Appropriate restraints or constraints were applied to the geometry and the atomic displacement parameters of the atoms in the cluster. All structures were examined using the Addsym subroutine of PLATON⁵⁴ to ensure that no additional symmetry could be applied to the models. Pertinent crystallographic data collection and refinement parameters are collated in Supplementary Table 4. Selected bond lengths and angles are collated in Supplementary Data 2.

Experiment details. *i*PrSH (Adamas-beta®) and CF_3COOAg (Adamas-beta®) were purchased from Shanghai Titan Scientific Co., Ltd. All other chemicals and solvents used in the syntheses were of analytical grade and used without further purification. IR spectra were recorded on a Perkin Elmer Spectrum Two in the frequency range of 4000–450 cm^{-1} . Powder X-ray diffraction (PXRD) patterns were recorded for microcrystalline powdered samples using a Rigaku Oxford Diffraction XtaLAB Synergy-S diffractometer using Cu radiation ($\lambda = 1.54184 \text{ \AA}$). The PXRD patterns were processed with the *CrystAlisPro* software suite using the Powder function⁵⁰. ³¹P NMR spectra were recorded in J. Young NMR tube on Bruker Avance 300 MHz spectrometer. UV-Vis spectra were performed on UV-Vis spectrophotometer (Evolution 220, ISA-220 accessory, Thermo Scientific). Temperature-dependent photoluminescence measurements were carried out in an Edinburgh spectrofluorimeter (FLS920) coupled with an Optistat DN cryostat (Oxford Instruments), and the ITC temperature controller and a pressure gauge were used to realize the variable-temperature measurement in the range of 113–293 K. Spectra were collected at different temperatures after a 5 min homiothermy. Time-resolved photoluminescence lifetime measurements were measured on Edinburgh spectrofluorimeter (FLS920) using a time-correlated single-photon counting technique. Mass spectra were recorded on an Agilent 6224 (Agilent Technologies, USA) ESI-TOF-MS spectrometer. Sample solutions are infused by a syringe pump at 240 μ L/h. Data were acquired using the following settings: electrospray ionization in positive mode, capillary voltage was set at 3.5 kV (-) and fragmentor at 200 V. The nebulizer was set to 15 psi and the nitrogen drying gas was set to a flow rate of 4 L/min. Drying gas temperature was maintained at 150 °C. The data analyses of mass spectra were performed based on the isotope distribution patterns using Agilent MassHunter Workstation Data acquisition software (Version B.05.00). The reported *m/z* values represent monoisotopic mass of the most abundant peak within the isotope pattern. The HAADF-STEM experiments were carried out at 300 kV using ThermoFisher Spectra 300 scanning transmission electron microscope with a probe Cs-corrector.

Computational details. DFT calculations were performed with the Gaussian 16 suite of programs⁵⁵. To reduce the computational cost, the ligand-simplified Ag_{51} cluster [(PW_9O_{34})@ $Ag_{51}(CH_3S)_{25}(CF_3COO)_{17}(HCONH_2)_3(H_2O)_3$] was used as a model for **SD/Ag51b**. The ligand simplification by changing *i*PrS to CH_3S was done from the crystal structure of **SD/Ag51b** with GaussView and the resulting model cluster was directly used for the subsequent TD-DFT calculation. The B3PW91 hybrid density functional⁵⁶ was employed in the TD-DFT calculation. The Los Alamos valence double-zeta with Hay-Wadt ECPs (LanL2DZ) basis set⁵⁷ containing relativistic effects was employed for Ag and W atoms, and 6–31G basis set was used for other non-metal atoms. A total of 300 singlet states were chosen and the root was set as 1. Data for orbital composition analysis with Mulliken partition are from Gaussian 16 calculations and further processed with Multiwfn software⁵⁸. The most probable transitions were determined based on the oscillator

strength values and weights. The optical absorption spectrum was convoluted with a Gaussian line shape with a half-width at half-height of 0.25 eV.

Data availability

The data supporting the findings reported herein can be found in the manuscript, its supplementary Information, or from the authors upon request. The time-dependent density functional theory calculations of SD/Ag51b and the selected bond lengths (Å) and angles (°) for silver nanoclusters are provided with Supplementary Data 1 and 2, respectively. The X-ray crystallographic coordinates for structures reported in this article have been deposited at the Cambridge Crystallographic Data Centre, under deposition number CCDC: 2091982–2091984 for SD/Ag51b, SD/Ag72a, and SD/Ag72c. These data can be obtained free of charge from the Cambridge Crystallographic Data Centre via www.ccdc.cam.ac.uk/data_request/cif.

Received: 10 August 2021; Accepted: 7 March 2022;

Published online: 04 April 2022

References

- Chakrabarty, R., Mukherjee, P. S. & Stang, P. J. Supramolecular coordination: self-assembly of finite two- and three-dimensional ensembles. *Chem. Rev.* **111**, 6810–6918 (2011).
- Zhou, X.-P. et al. A high-symmetry coordination cage from 38- or 62-component self-assembly. *J. Am. Chem. Soc.* **134**, 8042–8045 (2012).
- Fujita, D. et al. Self-assembly of tetrahedral Goldberg polyhedra from 144 small components. *Nature* **540**, 563–566 (2016).
- Greenfield, J. L., Rizzuto, F. J., Goldberga, I. & Nitschke, J. R. Self-assembly of conjugated metallopolymers with tunable length and controlled regiochemistry. *Angew. Chem. Int. Ed.* **56**, 7541–7545 (2017).
- Zhang, G.-L., Zhou, L.-P., Yuan, D.-Q. & Sun, Q.-F. Bottom-up construction of mesoporous nanotubes from 78-component self-assembled nanobarrels. *Angew. Chem. Int. Ed.* **54**, 9844–9848 (2015).
- Wang, Z. et al. Assembly of silver Trigons into a buckyball-like Ag₁₈₀ nanocage. *Proc. Natl Acad. Sci. USA* **114**, 12132–12137 (2017).
- Gao, M.-Y. et al. Fullerene-like polyoxotitanium cage with high solution stability. *J. Am. Chem. Soc.* **138**, 2556–2559 (2016).
- Peng, J.-B. et al. Beauty, symmetry, and magnetocaloric effect—four-shell keplerates with 104 lanthanide atoms. *J. Am. Chem. Soc.* **136**, 17938–17941 (2014).
- Zhang, L., Clerac, R., Heijboer, P. & Schmitt, W. Influencing the symmetry of high-nuclearity and high-spin manganese oxo clusters: supramolecular approaches to manganese-based keplerates and chiral solids. *Angew. Chem. Int. Ed.* **51**, 3007–3011 (2012).
- Argent, S. P. et al. High-nuclearity metal-organic nanospheres: a Cd₆₆ ball. *J. Am. Chem. Soc.* **134**, 55–58 (2012).
- Kong, X.-J., Long, L.-S., Zheng, Z., Huang, R.-B. & Zheng, L.-S. Keeping the ball rolling: fullerene-like molecular clusters. *Acc. Chem. Res.* **43**, 201–209 (2010).
- Anson, C. E. et al. Synthesis and crystal structures of the ligand-stabilized over chalcogenide clusters [Ag₁₅₄Se₇₇(dppxy)₁₈], [Ag₃₂₀(StBu)₆₀S₁₃₀(dppp)₁₂], [Ag₃₅₂S₁₂₈(StC₅H₁₁)₉₆], and [Ag₄₉₀S₁₈₈(StC₅H₁₁)₁₁₄]. *Angew. Chem. Int. Ed.* **47**, 1326–1331 (2008).
- Mednikov, E. G., Jewell, M. C. & Dahl, L. F. Nonosized (μ₁₂-Pt)Pd_{164-x}Pt_x(CO)₇₂(PPh₃)₂₀ (x = 7) containing Pt-centered four-shell 165-atom Pd-Pt core with unprecedented intershell bridging carbonyl ligands: Comparative analysis of icosahedral shell-growth patterns with geometrically related Pd₁₄₅(CO)_x(PEt₃)₃₀ (x ≈ 60) containing capped three-shell Pd₁₄₅ core. *J. Am. Chem. Soc.* **129**, 11619–11630 (2007).
- Young, A. G. & Hanton, L. R. Square planar silver(I) complexes: a rare but increasingly observed stereochemistry for silver(I). *Coord. Chem. Rev.* **252**, 1346–1386 (2008).
- Schmidbaur, H. & Schier, A. Argentophilic interactions. *Angew. Chem. Int. Ed.* **54**, 746–784 (2015).
- Dhayal, R. S. et al. [Ag₂₁{S₂P(OiPr)₂]₁₂]⁺: an eight-electron superatom. *Angew. Chem. Int. Ed.* **54**, 3702–3706 (2015).
- Wang, S., Li, Q., Kang, X. & Zhu, M. Customizing the structure, composition, and properties of alloy nanoclusters by metal exchange. *Acc. Chem. Res.* **51**, 2784–2792 (2018).
- Diecke, M., Schrenk, C. & Schnepf, A. Synthesis and characterization of the highly unstable metalloid cluster Ag₆₄(PⁿBu₃)₁₆Cl₆. *Angew. Chem. Int. Ed.* **59**, 14418–14422 (2020).
- Jin, R., Zeng, C., Zhou, M. & Chen, Y. Atomically precise colloidal metal nanoclusters and nanoparticles: fundamentals and opportunities. *Chem. Rev.* **116**, 10346–10413 (2016).
- Friedfeld, M. R., Stein, J. L., Ritchhart, A. & Cossairt, B. M. Conversion reactions of atomically precise semiconductor clusters. *Acc. Chem. Res.* **51**, 2803–2810 (2018).
- Zeng, C., Chen, Y., Das, A. & Jin, R. Transformation chemistry of gold nanoclusters: from one stable size to another. *J. Phys. Chem. Lett.* **6**, 2976–2986 (2015).
- Nimmala, P. R. & Dass, A. Au₃₆(SPh)₂₃ nanomolecules. *J. Am. Chem. Soc.* **133**, 9175–9177 (2011).
- Hau, S. C. K., Cheng, P.-S. & Mak, T. C. W. Enlargement of globular silver alkyne cluster via core transformation. *J. Am. Chem. Soc.* **134**, 2922–2925 (2012).
- Huang, R.-W. et al. Hypersensitive dual-function luminescence switching of a silver-chalcogenolate cluster-based metal-organic framework. *Nat. Chem.* **9**, 689–697 (2017).
- Liu, H. et al. Acid-base-triggered structural transformation of a polyoxometalate core inside a dodecahedrane-like silver thiolate shell. *Angew. Chem. Int. Ed.* **55**, 3699–3703 (2016).
- Wang, Z., Su, H.-F., Tung, C.-H., Sun, D. & Zheng, L.-S. Deciphering synergetic core-shell transformation from [Mo₆O₂₂@Ag₄₄] to [Mo₈O₂₈@Ag₅₀]. *Nat. Commun.* **9**, 4407 (2018).
- Zheng, S.-T. & Yang, G.-Y. Recent advances in paramagnetic-TM-substituted polyoxometalates (TM = Mn, Fe, Co, Ni, Cu). *Chem. Soc. Rev.* **41**, 7623–7646 (2012).
- Wang, J. et al. A novel type of heteropolyoxoanion precursors {[Ca(H₂O)₆][P₄M₆O₃₄]₁₂¹²⁻ (M = W^{VI}, Mo^{VI})} constructed by two [P₄M₆O₃₄]₁₂¹²⁻ subunits via a rare hexa-calcium cluster. *Chem. Commun.* 2362–2364, <https://doi.org/10.1039/B822368H> (2009).
- Zheng, S.-T., Zhang, J., Clemente-Juan, J. M., Yuan, D.-Q. & Yang, G.-Y. Poly(polyoxotungstate)s with 20 nickel centers: from nanoclusters to one-dimensional chains. *Angew. Chem. Int. Ed.* **48**, 7176–7179 (2009).
- Zheng, S.-T., Zhang, H. & Yang, G.-Y. Designed synthesis of POM-organic frameworks from {Ni₆PW₆} building blocks under hydrothermal conditions. *Angew. Chem. Int. Ed.* **47**, 3909–3913 (2008).
- Jiang, Z.-G., Shi, K., Lin, Y.-M. & Wang, Q.-M. [Ag₇₀(PW₉O₃₄)₂(^tBuC≡C)₄₄(H₂O)₂]⁸⁺: ionothermal synthesis of a silver cluster encapsulating lacunary polyoxometalate ions. *Chem. Commun.* **50**, 2353–2355 (2014).
- Yan, B.-J. et al. Self-Assembly of a Stable Silver Thiolate Nanocluster Encapsulating a Lacunary Keggin Phosphotungstate Anion. *Inorg. Chem.* **57**, 4828–4832 (2018).
- Liu, K.-G. et al. The transformation of polyoxometalates in the formation of intercluster compound [Ag₄₁(α-SiW₁₀O₃₇)(^tBuC≡C)₂₇(CH₃CN)₅][β-SiW₁₂O₄₀]. *Chem. Commun.* **52**, 3801–3804 (2016).
- Duan, G.-X. et al. High-nuclearity heterometallic *tert*-butylethynyl clusters assembled with *tert*-butylphosphonate. *Chem.-Eur. J.* **24**, 6762–6768 (2018).
- Long, D.-L., Tsunashima, R. & Cronin, L. Polyoxometalates: building blocks for functional nanoscale systems. *Angew. Chem. Int. Ed.* **49**, 1736–1758 (2010).
- Xuan, W. et al. Stereoselective assembly of gigantic chiral molybdenum blue wheels using lanthanide ions and amino acids. *J. Am. Chem. Soc.* **141**, 1242–1250 (2019).
- Zheng, Q. et al. Self-sorting of heteroatoms in the assembly of cross-shaped polyoxometalate clusters. *J. Am. Chem. Soc.* **140**, 2595–2601 (2018).
- Yao, Q. et al. Understanding seed-mediated growth of gold nanoclusters at molecular level. *Nat. Commun.* **8**, 927 (2017).
- Yao, Q. et al. Precise control of alloying sites of bimetallic nanoclusters via surface motif exchange reaction. *Nat. Commun.* **8**, 1555 (2017).
- Goswami, N., Yao, Q., Chen, T. & Xie, J. Mechanistic exploration and controlled synthesis of precise thiolate-gold nanoclusters. *Coord. Chem. Rev.* **329**, 1–15 (2016).
- Hu, Y.-Q. et al. Tracking the formation of a polynuclear Co₁₆ complex and its elimination and substitution reactions by mass spectroscopy and crystallography. *J. Am. Chem. Soc.* **135**, 7901–7908 (2013).
- Cao, Y. et al. Reversible isomerization of metal nanoclusters induced by intermolecular interaction. *Chem* **7**, 2227–2244 (2021).
- Kang, X. & Zhu, M. Tailoring the photoluminescence of atomically precise nanoclusters. *Chem. Soc. Rev.* **48**, 2422–2457 (2019).
- Yam, V. W.-W., Au, V. K.-M. & Leung, S. Y.-L. Light-emitting self-assembled materials based on d⁸ and d¹⁰ transition metal complexes. *Chem. Rev.* **115**, 7589–7728 (2015).
- Barbieri, A., Accorsi, G. & Armaroli, N. Luminescent complexes beyond the platinum group: the d¹⁰ avenue. *Chem. Commun.* **2008**, 2185–2193 (2008).
- Santiago-Gonzalez, B. et al. Permanent excimer superstructures by supramolecular networking of metal quantum clusters. *Science* **353**, 571–575 (2016).
- Zhang, Z. & Ren, S. Metal-cluster-based colloidal excimer superstructures. *Angew. Chem. Int. Ed.* **55**, 15708–15710 (2016).
- Santiago-Gonzalez, B. et al. Bottom-up synthesis and self-assembly of copper clusters into permanent excimer supramolecular nanostructures. *Angew. Chem. Int. Ed.* **57**, 7051–7055 (2018).
- Domaille, P. J., Hervé, G. & Téazé, A. *Inorg. Synth.* **27**, 96–104 (1990).

50. Rigaku Oxford Diffraction. *CrysAlis^{Pro} Software System* version 1.171.40.25a (Rigaku Corporation, 2018).
51. Palatinus, L. & Chapuis, G. SUPERFLIP—a computer program for the solution of crystal structures by charge flipping in arbitrary dimensions. *J. Appl. Crystallogr.* **40**, 786–790 (2007).
52. Sheldrick, G. M. Crystal structure refinement with SHELXL. *Acta Crystallogr. C* **71**, 3–8 (2015).
53. Dolomanov, O. V., Bourhis, L. J., Gildea, R. J., Howard, J. A. K. & Puschmann, H. OLEX2: a complete structure solution, refinement and analysis program. *J. Appl. Crystallogr.* **42**, 339–341 (2009).
54. Spek, A. L. Structure validation in chemical crystallography. *Acta Crystallogr. D* **65**, 148–155 (2009).
55. Frisch, M. et al. *Gaussian 16* Rev. B. 01 (Gaussian, Inc., 2016).
56. Adamo, C. & Barone, V. Exchange functionals with improved long-range behavior and adiabatic connection methods without adjustable parameters: The *mPW* and *mPW1PW* models. *J. Chem. Phys.* **108**, 664–675 (1998).
57. Hay, P. J. & Wadt, W. R. *Ab initio* effective core potentials for molecular calculations. Potentials for K to Au including the outermost core orbitals. *J. Chem. Phys.* **82**, 299–310 (1985).
58. Lu, T. & Chen, F. Multiwfn: a multifunctional wavefunction analyzer. *J. Comput. Chem.* **33**, 580–592 (2012).

Acknowledgements

This work was financially supported by the National Natural Science Foundation of China (Grant Nos. 22171164, 91961105, 21822107, 21827801), the Fok Ying Tong Education Foundation (171009), the Natural Science Foundation of Shandong Province (Nos. ZR2020ZD35 and ZR2019ZD45), the Taishan Scholar Project of Shandong Province of China (Nos. tsqn201812003 and ts20190908), the Qilu Youth Scholar Funding of Shandong University, the National Postdoctoral Innovative Talents Support Program (No. BX2021171), China Postdoctoral Science Foundation (No. 2021M700081), Project for Scientific Research Innovation Team of Young Scholar in Colleges and Universities of Shandong Province (No. 2019KJC028).

Author contributions

D.S. conceived and designed the experiments; Z.W. and Y.J.Z. conducted synthesis and characterization; Z.W. and D.S. performed research and analyzed data; J.M.D., Z.Y.G., and C.H.T. contributed to scientific discussion; Y.Z.L. and G.L.Z. performed the DFT

calculations; K.P.S. collected the HAADF-STEM images; D.S., M.K., and Z.W. wrote the paper. All authors discussed the results and commented on the manuscript.

Competing interests

The authors declare no competing interests.

Additional information

Supplementary information The online version contains supplementary material available at <https://doi.org/10.1038/s41467-022-29370-w>.

Correspondence and requests for materials should be addressed to Di Sun.

Peer review information *Nature Communications* thanks Yongge Wei and the other, anonymous, reviewer(s) for their contribution to the peer review of this work.

Reprints and permission information is available at <http://www.nature.com/reprints>

Publisher's note Springer Nature remains neutral with regard to jurisdictional claims in published maps and institutional affiliations. Reprint and permissions information is available at <http://www.nature.com/>.



Open Access This article is licensed under a Creative Commons Attribution 4.0 International License, which permits use, sharing, adaptation, distribution and reproduction in any medium or format, as long as you give appropriate credit to the original author(s) and the source, provide a link to the Creative Commons license, and indicate if changes were made. The images or other third party material in this article are included in the article's Creative Commons license, unless indicated otherwise in a credit line to the material. If material is not included in the article's Creative Commons license and your intended use is not permitted by statutory regulation or exceeds the permitted use, you will need to obtain permission directly from the copyright holder. To view a copy of this license, visit <http://creativecommons.org/licenses/by/4.0/>.

© The Author(s) 2022